Microscopy and Microanalysis (2022), **28**, 672–679
doi:10.1017/S143192762200040X

Microscopy AND Microanalysis

Original Article

Localized Phonon Densities of States at Grain Boundaries in Silicon

Peter Rez[1]*, Tara Boland[2], Christian Elsässer[3] and Arunima Singh[1]

[1]Department of Physics, Arizona State University, Tempe, AZ 85287-1504, USA; [2]School For Engineering of Matter Transport and Energy, Arizona State University, Tempe, AZ 85287-6106, USA and [3]Fraunhofer Institute for Mechanics of Materials IWM, Wöhlerstraße 11, 79108 Freiburg, Germany

Abstract

Since it is now possible to record vibrational spectra at nanometer scales in the electron microscope, it is of interest to explore whether extended defects in crystals such as dislocations or grain boundaries will result in measurable changes of the phonon densities of states (dos) that are reflected in the spectra. Phonon densities of states were calculated for a set of high angle grain boundaries in silicon. The boundaries are modeled by supercells with up to 160 atoms, and the vibrational densities of states were calculated by taking the Fourier transform of the velocity–velocity autocorrelation function from molecular dynamics simulations with larger supercells doubled in all three directions. In selected cases, the results were checked on the original supercells by comparison with the densities of states obtained by diagonalizing the dynamical matrix calculated using density functional theory. Near the core of the grain boundary, the height of the optic phonon peak in the dos at 60 meV was suppressed relative to features due to acoustic phonons that are largely unchanged relative to their bulk values. This can be attributed to the variation in the strength of bonds in grain boundary core regions where there is a range of bond lengths.

Key words: DFT (density functional theory), EELS (electron energy-loss spectroscopy), grain boundary, localized phonon, MD (molecular dynamics)

(Received 1 November 2021; revised 4 February 2022; accepted 1 March 2022)

Introduction

Recent developments in monochromators and electron energy loss spectrometers for transmission electron microscopy have made it possible to record vibrational spectra, potentially at nanometer resolution, in the electron microscope (Krivanek et al., 2014). Atomic resolution images at energies corresponding to vibrational modes or phonons have been demonstrated in BN (Hage et al., 2019) and Si (Venkatraman et al., 2019), by selecting phonon wave vectors corresponding to localized or impact scattering. This raises the intriguing possibility of experimentally measuring localized phonon modes at extended structural defects in crystals and using measured local densities of states to investigate how defects may change important macroscopic thermal transport properties such as thermal conductivity. Localized modes associated with a single silicon atom in a graphene sheet have been observed by Hage et al. (2020), and a change in phonon density of states (DOS) corresponding to a stacking fault in 3C SiC was reported by Yan et al. (2021).

Localized modes associated with a point defect, namely an atom with a different mass, are to be expected, though the spectacular result of Yan et al. (2021) showing an observable change at a stacking fault in 3C SiC could be a consequence of the stacking fault being a two layer region of 2H SiC, a different polytype. Although grain boundaries (GBs) or dislocations should give rise to differences in the phonon DOS, it is still not certain whether they would be detectable unequivocally. An energy resolution of 5 meV or 40 cm^{-1} has been achieved using the monochromator spectrometer combination in the Nion HERMES Ultra STEM electron microscope. This is a significant advance on what has been achieved in the past, but still very much inferior to what is possible with infrared absorption or Raman spectroscopy on bulk specimens.

Ziebarth et al. (2015) and Stoffers et al. (2015) performed first-principles calculations, using density functional theory (DFT), to determine the atomic positions in supercells representing various GBs in silicon. For a Σ 9 boundary, Stoffers et al. (2015) also compared the DFT results with high-resolution scanning transmission electron microscopy images.

We used the atomic coordinates of the structurally relaxed GB models of Ziebarth et al. (2015) and Stoffers et al. (2015) to calculate the phonon DOS in two ways: by enumerating the modes obtained by diagonalizing the dynamical matrix, calculated directly by DFT; by taking the Fourier transform of the velocity–velocity correlation function of the atoms in an extended molecular dynamics (MD) simulation. In calculating the DOS, we made a distinction between those atoms at the GB core and those that were in regions that can be considered as similar to the bulk Si crystal. In all considered cases but one (see section Results and Discussion), the peak in the DOS at 60 meV was depressed for atoms in the core region.

Theory

Phonons are the quantized vibrations of the atoms in the crystal lattice; they are uniquely determined by their wave vector in the first Brillouin Zone and their polarization vector.

*Corresponding author: Peter Rez, E-mail: peter.rez@asu.edu

Cite this article: Rez P, Boland T, Elsässer C, Singh A (2022) Localized Phonon Densities of States at Grain Boundaries in Silicon. *Microsc Microanal* **28**, 672–679. doi:10.1017/S143192762200040X

The appropriate theory for electron scattering by individual phonon modes applied to high-resolution imaging in perfect silicon crystals has been published by Rez & Singh (2021). Other theoretical formulations have also been applied to high-resolution imaging in phonon modes. Forbes et al. (2010, 2016) extended their earlier model based on a quantum mechanical treatment with an Einstein phonon dispersion. More recently, Zeiger & Rusz (2020, 2021*a*) have published a theoretical framework based on MD sampling of phonon modes where the frequency is selected using a delta thermostat. They applied their theory to imaging antiphase boundaries in BN (Zeiger & Rusz, 2021*b*). Since the GB systems that we are studying are represented by large supercells, the Brillouin Zone is relatively small, and as a first approximation, the DOS needs only to be evaluated by enumerating the frequencies at the Γ point (or typically only a small number of k points) (Ashcroft & Mermin, 1976). From Rez & Singh (2021), the intensity $I(\mathbf{r_p},t)$ for a large supercell of thickness t as a function of probe position $\mathbf{r_p}$ is given by the following equation:

$$I(\mathbf{r_p},t)=\iint\left|\int R_{MS}(t-z)H(q)P_{MS}(z)*A(\mathbf{r_p})dz\right|^2 d^2q, \quad (1)$$

where z is a depth, P_{MS} and R_{MS} represent the propagation of the elastic wavefield before and after phonon scattering by wavevector $\mathbf{q}$, and A is the probe amplitude in real space. The phonon scattering operator $H(\mathbf{q})$ for creation a phonon frequency $\omega(q)$ is given by the following equation:

$$H(\boldsymbol{q})=\boldsymbol{q}.\boldsymbol{e}\left(\frac{\hbar}{2Ma\omega(q)}\right)^{\frac{1}{2}}\left(1+N_{\mathrm{BE}}\left(\frac{\hbar\,\omega(q)}{kBT}\right)\right)^{\frac{1}{2}}f_{\mathrm{el}}(q)N, \quad (2)$$

where $\mathbf{e}$ is the polarization, M_a is the mass of the atom, N_{BE} is the Bose Einstein factor for a phonon of frequency $\omega(q)$ at temperature T, k_B is Boltzmann's constant, N is the number of atoms in the supercell, and $f_{\mathrm{el}}(q)$ is the electron scattering factor. The dominant contribution to the intensity is the variation with inverse of the phonon frequency, and since the Brillouin Zone is small, we are effectively sampling the phonon DOS, for which we need the frequencies of the $3N$ modes. The scalar product of wave vector with polarization acts to sample displacements in the plane of the specimen. The measured EELS spectrum, therefore, strongly resembles the appropriate local projected phonon DOS, as confirmed by the extensive calculations of Zeiger & Rusz (2021*b*).

The frequencies are obtained by diagonalizing the dynamical matrix D

$$D\begin{pmatrix} k & \\ b & b' \\ \alpha & \alpha' \end{pmatrix}=\frac{e^{-i\mathbf{k}.\mathbf{R}_{b'}}}{\sqrt{M_{b'}}}\phi\begin{pmatrix} b & b' \\ \alpha & \alpha' \end{pmatrix}\frac{e^{i\mathbf{k}.\mathbf{R}_b}}{\sqrt{M_b}}, \quad (3)$$

where b labels atoms of mass M_b in the simulation cell with periodic boundary conditions, α labels the polarization and $\boldsymbol{\Phi}$ is the force-constant matrix, and k is the wave vector. The number of modes is $3N$, where N is the number of atoms in the unit cell. The original supercells that represent our GBs contain up to 160 atoms; thus, the dynamical matrix can be of size up to 480×480. All DFT calculations were done using the projector augmented-wave method as implemented in the plane-wave code VASP (Kresse & Furthmüller, 1996*a*, 1996*b*; Kresse & Joubert, 1999) within the generalized gradient approximation of Perdew, Burke, and Ernzerhof for exchange-correlation (Perdew et al., 1996). A plane-wave energy cutoff of 400 eV was used. A k-point sampling mesh with at least 10 points/Å was used for the supercells together with a 0.01 eV smearing width of the Gaussian smearing scheme. The GB models of Ziebarth et al. (2015) and Stoffers et al. (2015) were re-relaxed using the aforementioned parameters. These settings were sufficient to converge all five GB cells to a total force per atom of less than 0.05 eV/ Å or better and an energy tolerance of 10^{-5} eV. A compilation of the lattice parameters of the cells, and the numbers of atoms is given in Table 1. Phonon calculations were performed using the direct finite-difference method (Frank et al., 1995; Kresse et al., 1995) implemented within the Phonopy package (Togo & Tanaka, 2015). To obtain the projected phonon DOS, a $1\times1\times1$ supercell approach was used for all GB cells with a $10\times10\times10$ k-point sampling mesh density. Finite atomic displacements of 0.01 Å were applied to calculate the force-constant matrix. The atomic displacements of the phonon modes, obtained from the eigenvectors of the modes at the Gamma point, were visualized using the v_sim code (https://gitlab.com/l_sim/v_sim).

An alternative method to calculate the phonon DOS is to take the Fourier transform of the velocity–velocity correlation function from MD trajectories of the atoms (Wang et al., 1989, 1990; Haas et al., 1999). The instantaneous velocities are determined by the differences in the atom positions in the time evolution of the MD trajectories. In practice, it was found to be beneficial to break the trajectory into L time slices of M steps and average over the resulting spectra. The phonon DOS $I(\omega_k)$ is given by the following equation:

$$I(\omega_k)=\frac{1}{L}\sum_{l=0}^{l=L-1}\sum_{j=2+lM}^{j=(l+1)M}\exp(i\omega_k t_j)\sum_{i=1}^{i=p}\sum_{n=1}^{n=N}v_{in}(t_j)v_{in}(t_2)\exp\left(-\frac{\sigma^2t_j^2}{4}\right), \quad (4)$$

where $v_{ik}(t_j)$ is proportional to the velocity at time t_j

$$v_{ik}(t_j)=u_{ik}(t_j)-u_{ik}(t_{j-1}), \quad (5)$$

and M is the number of time steps in each time slice l, t_j is the jth time step, N is the number of atoms, ω_k is a frequency, and u_i is the coordinate in the ith direction (x,y,z) for atom k. For the total DOS, it is summed over dimensions x, y, and z ($p=3$). The parameter σ is related to the instrumental broadening, ΔE by

$$\sigma=\frac{\Delta Ee}{2\hbar\sqrt{\ln 2}}, \quad (6)$$

when ΔE is in eV.

This approach was proposed by Beeman & Alben (1977) and has been used to calculate the thermal conductivity of MgO by de Koker (2009), phonon dispersions and lifetimes in carbon nanotubes by Thomas et al. (2010), and infrared spectra of large proteins by Mott et al. (2013). This is also very similar to the procedure used by Zeiger & Rusz (2020, 2021*a*), though we do not use a δ thermostat to select a particular range of phonon frequencies.

Scattering wave vectors in electron energy-loss spectroscopy (EELS) in the electron microscope are predominately in the plane of the specimen, normal to the incident beam. For densities of states that would be observed by EELS in the electron microscope, the displacement direction, i, is only summed over the two dimensions in the plane of the specimen ($p=2$). The

https://doi.org/10.1017/S143192762200040X Published online by Cambridge University Press

Table 1. Compilation of Numbers of Atoms and Unit Cell Parameters of the Supercells for the Five Investigated GBs.

	Σ3 (112) Mirror-symmetric	Σ3 (112) Non-symmetric	Σ5 (130)	Σ5 (120)	Σ9 (221)
No. of atoms in DFT supercell	144	136	40	160	68
No. of atoms in MD supercell	1,152	1,088	320	1,280	544
a (Å)	9.4790	9.4336	5.3335	12.3261	11.6531
b (Å)	40.5757	38.7540	17.6788	24.5705	31.0746
c (Å)	7.6715	7.6715	8.7036	10.8160	3.8576

The "large" MD supercells contain $2^3 = 8$ times as many atoms and have unit-cell parameters twice as long.

specimen's surface plane normal for the Σ 3 and Σ9 boundaries in Figure 1 is (110), which is the most frequently used orientation for high-resolution electron microscopy of silicon (Krivanek & Maher, 1978; Smith, 2020). There have been fewer high-resolution electron microscopy results for the (100) orientation which is the specimen normal for the Σ 5 boundaries (Ourmazd et al., 1985).

MD simulations were performed with the LAMMPS (Plimpton, 1995) package using the phonon fix command that measures the elastic Green's function by making use of the fluctuation–dissipation theorem implemented by Kong (2011) to obtain the phonon spectrum. The positions of atoms in the supercells of GBs determined by Ziebarth et al. (2015) and Stoffers et al. (2015) were used as the initial atom coordinates. In practice, it was found that their supercells were too small for calculating the phonon DOS. Various multiples of the supercell were tried, and it was found that convergence was achieved with a larger supercell containing the original supercells $2 \times 2 \times 2$ times. The numbers of atoms in these larger supercells are given in the second line of Table 1. These simulations were performed with periodic boundary conditions applied in all directions. The interaction among atoms was described using the Tersoff potential (Tersoff, 1989). The Nosé–Hoover style thermostat and barostat (Nose, 1984; Hoover, 1985; Klein et al., 1994; Müser & Binder, 2001) were employed to maintain the system at 300 K and 1 atmosphere. A time step of 1 fs was used with a total simulation time of 0.05 ns. The atom positions were saved at each time step. These computational settings were sufficient to obtain a stable spectrum. Additional convergence checks were performed for simulation times of 0.1 ns. For calculating the spectra as given by equations (2) and (3), the trajectories were divided into 24 blocks of 2,048 time steps, and the results were averaged. All spectra were normalized using the constraint that there are three vibrational modes per atom.

Calculating phonon DOS by DFT and Phonopy for the supercells, as shown in Figure 1, is computer resource and time-intensive. This was only done for selected cases as a way of checking and validating the results from the analysis of MD trajectories by direct comparison with the calculation of the phonon spectrum from the dynamical matrix.

Results and Discussion

To validate the MD approach, in particular the Tersoff potential we used, we compared the phonon DOS calculated by both MD

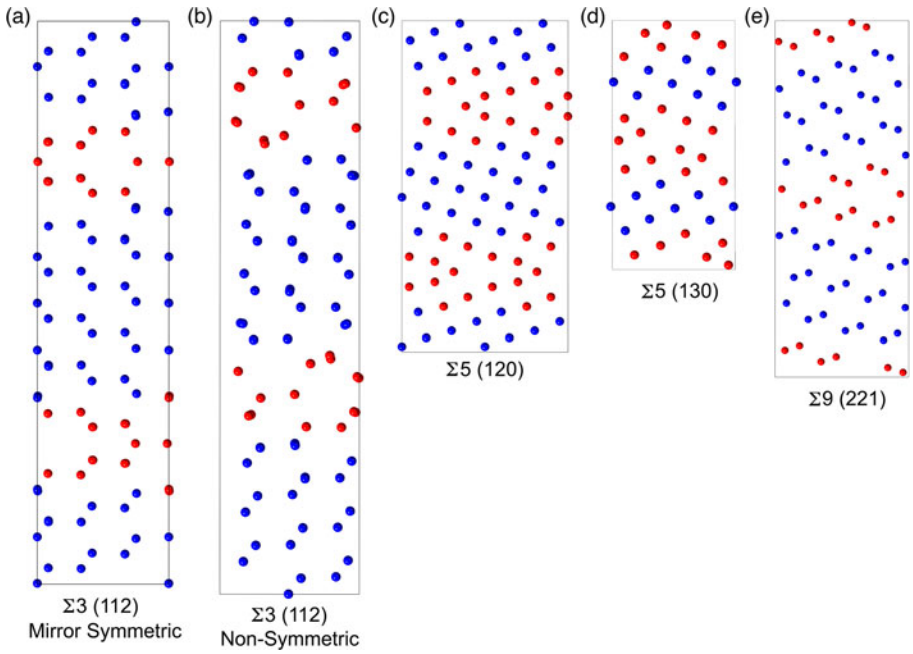

Fig. 1. The original DFT supercells for the various GBs. The atoms at the GB core are shown as red circles and the "bulk" atoms are shown as blue circles.

https://doi.org/10.1017/S143192762200040X Published online by Cambridge University Press

and by diagonalizing the dynamical matrix using VASP in association with Phonopy. The result for a perfect crystal is shown in Figure 2a. The most prominent feature is the peak in the DOS at 60 meV. Silicon has an optic mode since there are two atoms in each primitive unit cell. There is little dispersion with wave vector for optic modes, which means they make a large contribution to the DOS. The peaks and their relative heights are the same, though the peaks in the DOS calculated using MD trajectories with the Tersoff potential are shifted to slightly higher energies. This is not unexpected, a similar shift was reported by Rohskopf et al. (2017). However, the strong similarity between the results of the two different approaches suggests that taking the Fourier transform of the velocity–velocity correlation function of instantaneous velocities from MD trajectories is a valid approach. It is conceivable that since the Tersoff potential was constructed originally for the perfect crystal structure, it might be of limited validity for the distorted structures at GBs. We performed DFT (VASP & Phonopy) calculations for the Σ 3 (112) mirror-symmetric boundary, Figure 2b, the Σ 5 (130) boundary, Figure 2c, and the Σ 9 (221) boundary, Figure 2d. These were intentionally chosen to span the range of changes in peak heights obtained by the MD calculations. The densities of states at boundaries calculated using MD with the Tersoff potential also show a shift to higher energies, similar to the shift observed for the perfect crystal. However, the similarity between the results of the MD calculations with the Tersoff potential and the results of the DFT calculations gives us confidence that the MD approach is valid for boundary structures, with considerable savings in computer time.

Figures 3–5 display comparisons between the total phonon DOS and the projected DOS that would be observed by EELS

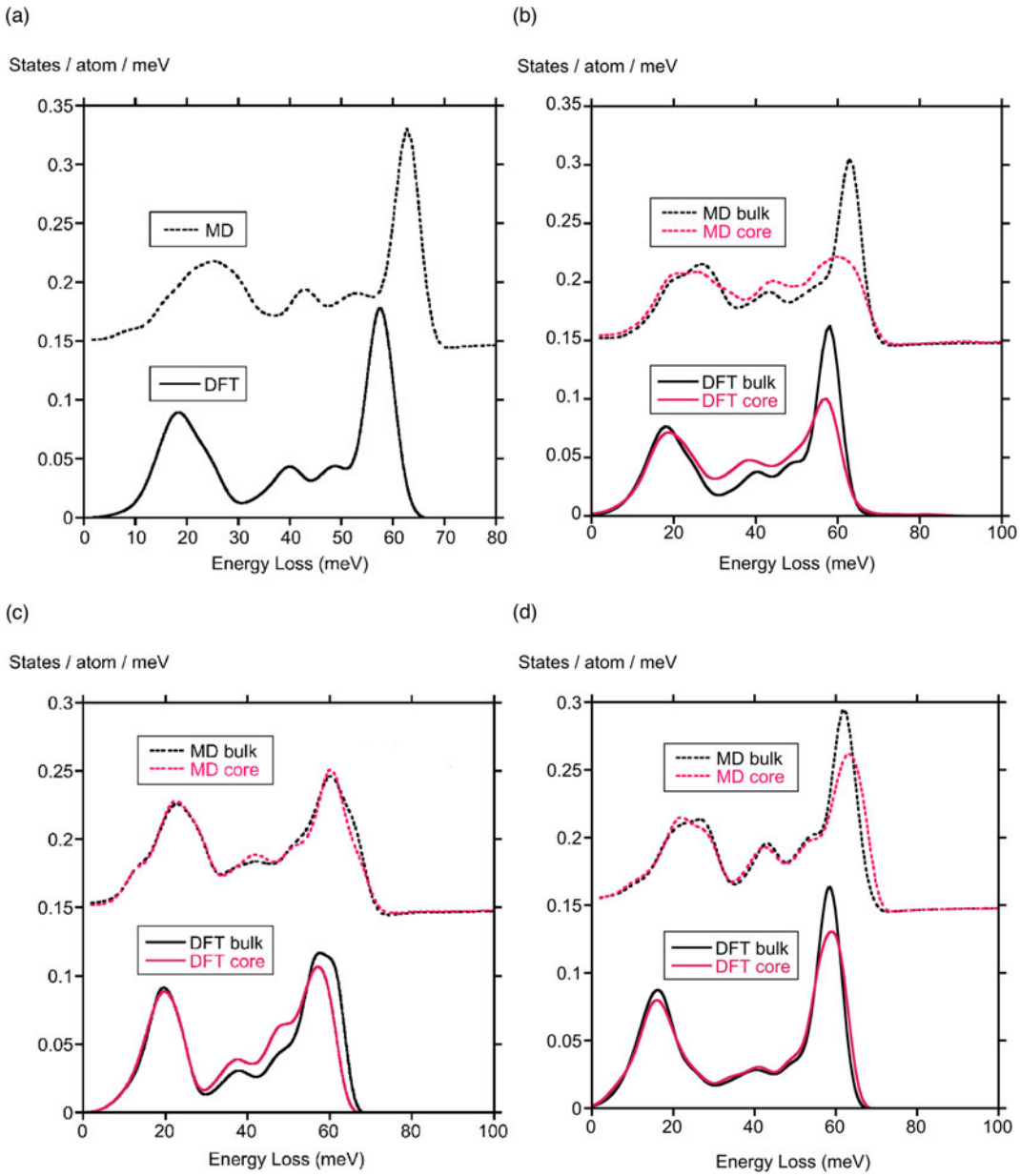

Fig. 2. Phonon DOS calculated with DFT (using VASP and Phonopy), and from MD trajectories obtained with LAMPPS and the Tersoff potential for (**a**) perfect crystal Si, (**b**) Σ 3 mirror-symmetric boundary, (**c**) Σ 5 (130) boundary, and (**d**) Σ 9 (221) boundary.

https://doi.org/10.1017/S143192762200040X Published online by Cambridge University Press

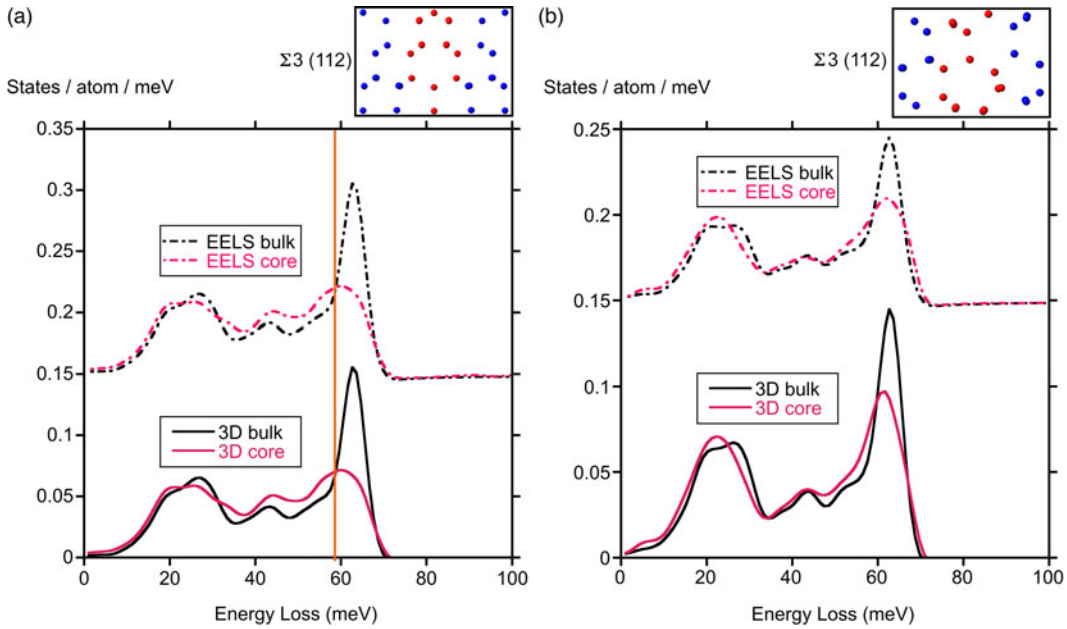

Fig. 3. Phonon densities of states and densities of states observed by EELS for Σ 3 (112) GBs. (**a**) Mirror-symmetric boundary and (**b**) non-symmetric boundary. The orange line marks the energy of the mode as shown in Figure 6a.

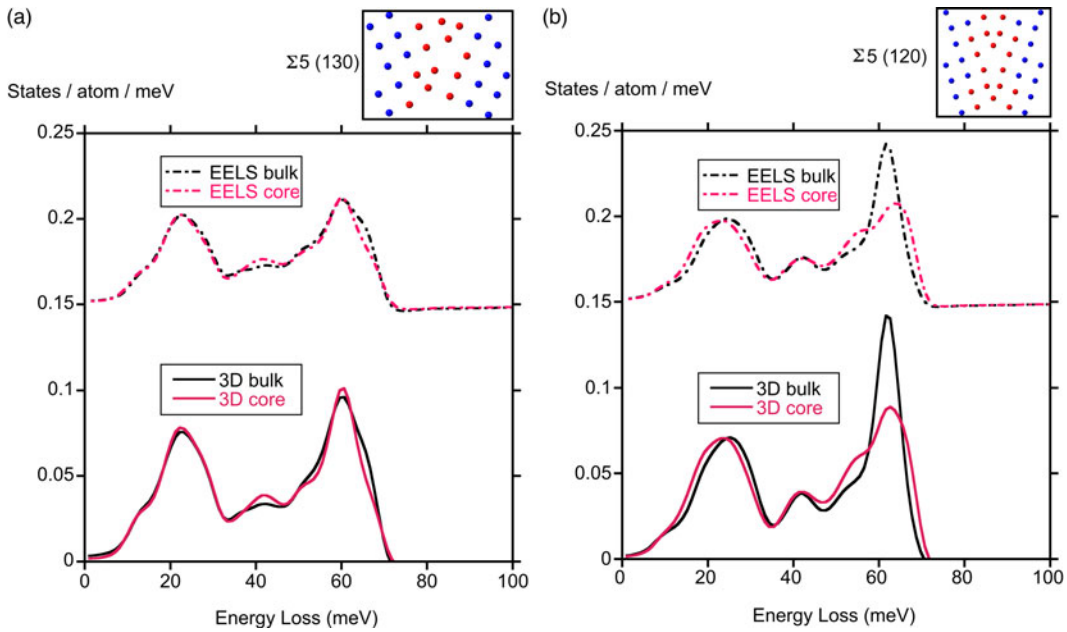

Fig. 4. Phonon densities of states for and densities of states observed by EELS Σ 5 GBs. (**a**) Σ 5 (130) boundary and (**b**) Σ 5 (120) boundary.

for atoms that are part of a GB (*core* atoms) and those that are more distant from the boundary (*bulk* atoms). The core and bulk atoms are marked as red and blue circles, respectively, in Figure 1. In all the graphs, the DOS is broadened by a Gaussian of 5 meV full width at half maximum (FWHM) to represent the instrumental energy resolution that can now be achieved in a transmission electron microscope. Given that it is possible to record spectra from regions as small as 0.5 nm, it should be possible to acquire distinct spectra representative of the core and bulk regions.

In all cases, the most significant and observable change is the reduction of the height of the optic-phonon peak in the DOS at 60 meV. The magnitude of the reduction in peak height is different for the different boundaries. It is greatest for the Σ 3 (112) mirror-symmetric boundary, Figure 3a, and hardly noticeable for the Σ5 (130) boundary, Figure 4a. The effect for the boundary with the lowest tilt angle (or highest sigma value) considered, the Σ 9 (221) boundary, Figure 5, is somewhere in between that for the Σ 3 (112) mirror-symmetric boundary, Figure 3a, and the Σ 5 (130) boundary, Figure 4a. It is

https://doi.org/10.1017/S143192762200040X Published online by Cambridge University Press

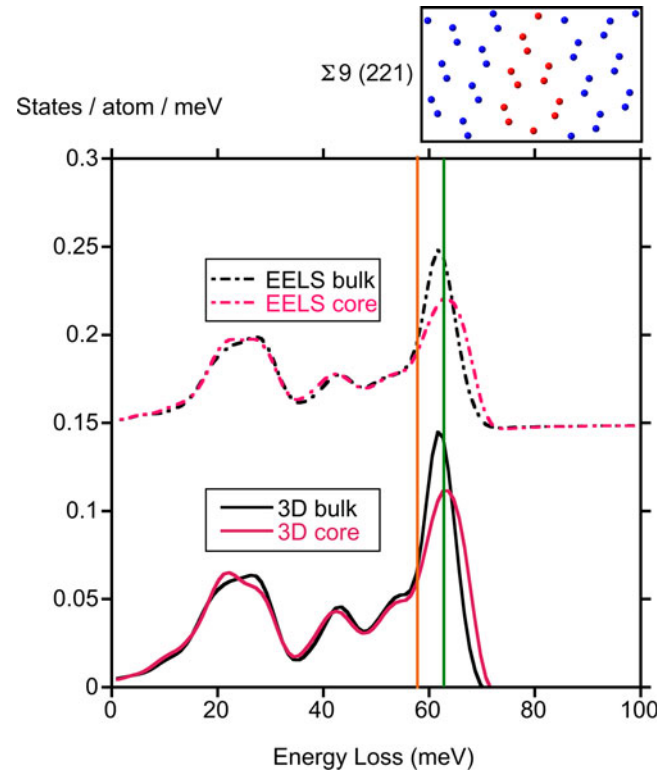

Fig. 5. Phonon DOS results and densities of states observed by EELS for the Σ 9 (221) GB. The orange line marks the energy of the mode as shown in Figure 6b, and the green line marks the energy of the mode as shown in Figure 6c.

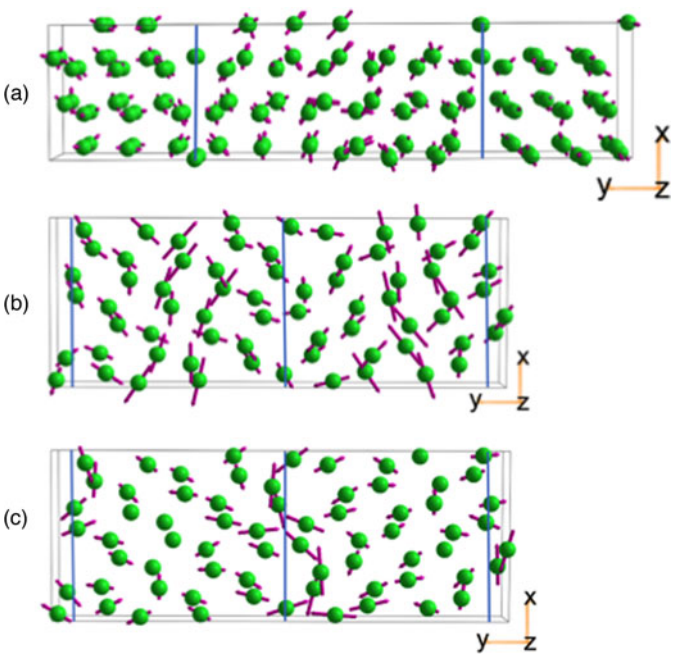

Fig. 6. Atomic displacements for modes predominately affecting bulk like atoms for (**a**) the 59 meV mode for the Σ 3 (112) boundary and (**b**) the 58 meV mode for the Σ 9 (221) boundary, (**c**) is a mode at 63 meV localized on boundary core atoms of the Σ 9 (221) boundary. The blue lines mark the locations of the boundary planes in the supercells.

interesting to note that the projected DOS that would be observed by EELS in the electron microscope is very similar to the total DOS. The magnitude of the DOS in states/atom/meV is two-thirds of the 3D DOS, as EELS selects a 2D projection.

The magnitude of the peak at 60 meV is controlled by the angle of the boundary and the Coincidence Site Lattice misorientation, as measured by the parameter Σ. The nature of the boundary plane can have a significant effect as shown by the difference between the peak height for the Σ 5 (130), Figure 4a, and Σ 5 (120) boundary, Figure 4b, and between the Σ 3 (112) boundaries with and without mirror symmetry, Figures 3a and 3b, respectively. However, for the supercell model of the Σ 5 (130) boundary shown in Figure 4a, the separation between the boundaries in the supercell was so small that most of the atoms are part of the boundary cores, as can be seen in Figure 1. Interatomic distances and angles vary considerably in the core regions of the GB, and this is reflected in the interatomic potential and the magnitude of the interatomic forces. This is very evident from the map of displacements for modes for the mirror-symmetric Σ 3 (112) and the Σ 9 (221) boundaries, as shown in Figures 6a and 6b, where the displacements are much smaller for atoms near the boundary core. The energies of these modes are marked as orange lines on the phonon DOS plots in Figures 3a and 5.

It is even more striking in the animations shown as movies S1 and S2 in the Supplementary material. Since the magnitude of the DOS is related to the size of the atomic displacements, as can be seen from equations (4) and (5), it is not surprising that the 60 meV optic phonon peak is reduced in both the total DOS and the projected DOS observed by EELS. There are relatively few modes localized to atoms at the core of the boundaries. There is a single mode at 63 meV for the Σ 9 (221) boundary, marked as a green line in Figure 5, with the displacements shown in Figure 6c. The animation is shown as movie S3 in the Supplementary material. However, it is unlikely that this single mode would be separately detected when the instrumental resolution is 5 meV.

To detect these changes at GBs, atomic resolution is not really necessary, and a probe size of 0.5–1 nm should be acceptable. In practice, a 10 mrad objective aperture semi-angle should be an appropriate setting. Since Venkatraman et al. (2019) have shown that it is possible to measure the phonon scattering at the atomic scale in Silicon using an on-axis detector, this should also work for detecting changes at the GB. The spectrometer entrance aperture should be chosen to maximize the collection efficiency, covering at least the first Brillouin Zone of the perfect crystal, yet at the same time not be so large that it results in a degradation of energy resolution. Appropriate setting of the projector lenses should achieve this objective. The ideal thickness (which might not be so easy to control) would maximize the (111) intensities so that Umklapp scattering from the second Brillouin Zone brings the phonon-scattered electrons back on the axis. Another possibility is to use an off-axis aperture centered on the second Brillouin Zone, but this is less than ideal as the collection efficiency is reduced. The ability to detect the reduction of the intensity of the 60 meV peak at GBs is most affected by the energy resolution that can be achieved. Figure 7 shows the effects of changing energy resolution, as defined by the FWHM of the zero-loss peak. The reduction of intensity is barely noticeable for 12 meV FWHM, and is not much more than 10% of the height of the peak for 9 meV FWHM, but is very apparent (about 30% of the height of the peak) for 5 meV FWHM. Although the lower contrast can be offset with more counts and a longer acquisition time, it would still be desirable to achieve an energy resolution between 5 and 7 meV.

https://doi.org/10.1017/S143192762200040X Published online by Cambridge University Press

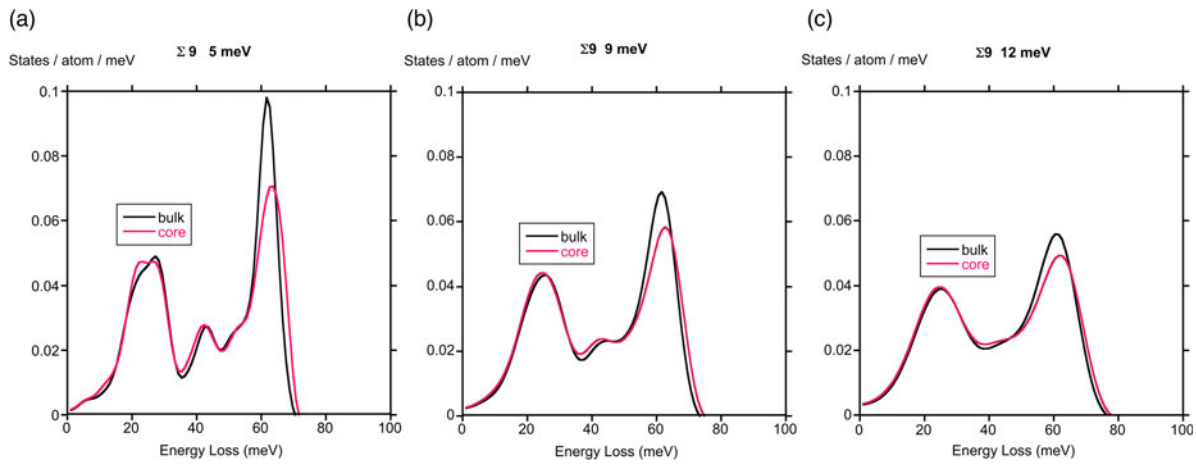

Fig. 7. Simulations of the densities of states that would be observed by EELS for the Σ9 (221) boundary for energy resolutions (as defined by the FWHM of zero-loss peak) of (**a**) 5, (**b**) 9, and (**c**) 12 meV.

Conclusions

Phonon densities of states in silicon calculated from velocity–velocity correlation functions of MD trajectories (using a Tersoff potential) were validated by comparison with those calculated directly from the dynamical matrix by DFT (using VASP and Phonopy). This agreement is not only true for perfect crystals but also for extended structural defects, namely GBs, where there might be concerns about the applicability of simple force fields. The phonon DOS due to optic phonons at 60 meV for Σ3 to Σ9 high-angle tilt boundaries is reduced compared to the optic phonon DOS in regions of bulk crystal structure. This change should be detectable by high-resolution EELS in electron microscopes in a specimen where the boundary plane is perpendicular to the specimen surface, and the electron beam runs parallel to the boundary core. The similarity between the densities of states from acoustic phonons at the boundary core and in bulk regions indicates that local changes of densities of states at the GBs cores should have minimal effect on the thermal conductivity of a polycrystalline microstructure of Si at ambient temperature. Any changes in thermal conductivity will be a consequence of phonon scattering at the GB leading to a reduction in phonon mean free paths.

Supplementary material. To view supplementary material for this article, please visit https://doi.org/10.1017/S143192762200040X.

Acknowledgment. T.B. and A.S. are supported in part by the Arizona State University start-up funds. A.S. is also funded by the NSF DMR under Grant No. 1906030 and as part of ULTRA, an Energy Frontier Research Center funded by the U.S. Department of Energy (DOE), Office of Science, Basic Energy Sciences (BES), under Award No. DE-SC0021230. This research used computational resources from the NSF-XSEDE under Award No. DMR150006, HPC resources from the Research Computing at Arizona State University, and computational resources from the National Energy Research Scientific Computing Center, a DOE Office of Science User Facility supported by the Office of Science of the U.S. Department of Energy under Contract No. DE-AC02-05CH11231.

Conflict of interest. The authors declare none.

References

Ashcroft NW & Mermin ND (1976). *Solid State Physics*. Orlando, FL: Harcourt Inc.

Beeman D & Alben R (1977). Vibrational properties of amorphous semiconductors. *Adv Phys* **26**(3), 339–361.

de Koker N (2009). Thermal conductivity of MgO periclase from equilibrium first principles molecular dynamics. *Phys Rev Lett* **103**, 125902.

Forbes BD & Allen LJ (2016). Modeling energy loss spectra due to phonon scattering. *Phys Rev B* **94**, 014110.

Forbes BD, Martin AV, Findlay SD, D'Alfonso AJ & Allen LJ (2010). Quantum mechanical model for phonon excitation in electron diffraction and imaging using a Born-Oppenheimer approximation. *Phys Rev B* **82**, 104103.

Frank W, Elsässer C & Fahnle M (1995). Ab initio force-constant method for phonon dispersions in alkali metals. *Phys Rev Lett* **74**(10), 1791–1794.

Haas H, Wang CZ, Ho KM, Fahnle M & Elsässer C (1999). Temperature dependence of the phonon frequencies of molybdenum: A tight-binding molecular dynamics study. *J Phys Condens Matter* **11**, 5455–5462.

Hage F, Kepaptsoglou DM, Ramasse QM & Allen LJ (2019). Phonon spectroscopy at atomic resolution. *Phys Rev Lett* **122**, 016103.

Hage FS, Radtke G, Kepaptsoglou DM, Lazzeri M & Ramasse QM (2020). Single-atom vibrational spectroscopy in the scanning transmission electron microscope. *Science* **367**(6482), 1124.

Hoover WG (1985). Canonical dynamics: Equilibriium phase-space distributions. *Phys Rev A* **31**, 1695–1197.

Klein ML, Martyna GJ & Tobias DJ (1994). Constant pressure molecular dynamics algoriths. *J Chem Phys* **101**, 4177.

Kong LT (2011). Phonon dispersion measured directly from molecular dynamics simulations. *Comput Phys Commun* **182**(10), 2201–2207.

Kresse G & Furthmüller J (1996*a*). Efficient iterative schemes for ab initio total-energy calculations using a plane-wave basis set. *Phys Rev B* **54**, 11169–11186.

Kresse G & Furthmüller J (1996*b*). Efficiency of ab-initio total energy calculations for metals and semiconductors using a plane-wave set. *Comput Mater Sci* **6**(1), 15–50.

Kresse G, Furthmüller J & Hafner J (1995). *Ab initio* force constant approach to phonon dispersion relations of diamond and graphite. *Europhys Lett* **32** (9), 729–734.

Kresse G & Joubert D (1999). From ultrasoft pseudopotentials to the projector augmented wave method. *Phys Rev B* **59**(3), 1758–1775.

Krivanek OL, Lovejoy TC, Delby N, Aoki T, Carpenter RW, Rez P, Soignard E, Zhu J, Batson PE, Lagos M, Egerton RF & Crozier PA (2014). Vibrational spectroscopy in the electron microscope. *Nature* **514**, 209–212.

Krivanek OL & Maher DM (1978). The core structure of extrinsic stacking faults in silicon. *Appl Phys Lett* **32**, 451–453.

Mott AJ, Thirumuruganandham SP, Thorpe MF & Rez P (2013). Fast calculation of the infrared spectra of large biomolecules. *Eur Biophys J Biophys Lett* **42**(11–12), 795–801.

Müser MH & Binder K (2001). Molecular dynamics study of the α–β transition in quartz: Elastic properties, finite size effects, and hysteresis in the local structure. *Phys Chem Minerals* **28**(10), 746–755.

Nose S (1984). A unified formulation of the constant temperature molecular dynamics method. *J Chem Phys* **117**(1), 511–519.

Ourmazd A, Ahlborn K, Ibeh K & Honda T (1985). Lattice and atomic structure imaging of semiconductors by high resolution transmission electron microscopy. *Appl Phys Lett* **47**(7), 685–688.

Perdew JP, Burke K & Ernzerhof M (1996). Generalized gradient approximation made simple. *Phys Rev Lett* **77**(18), 3865–3868.

Plimpton S (1995). Fast parallel algorithms for short range molecular dynamics. *J Comput Phys* **117**(1), 1–19.

Rez P & Singh A (2021). Lattice resolution of vibrational modes in the elctron microscope. *Ultramicroscopy* **220**, 113162.

Rohskopf A, Seyf HR, Gordiz K, Tadano T & Henry A (2017). Empirical interatomic potentials optimized for phonon properties. *Comput Mater* **3**, 27.

Smith DJ (2020). Atomic-resolution structure imaging of defects and interfaces in compound semiconductors. *Prog Cryst Growth Charact Mater* **66**, 100498.

Stoffers A, Ziebarth B, Barthel J, Cojocaru-Miredin O, Elsässer C & Raabe D (2015). Complex nanotwin substructure of an asymmetric Σ9 tilt grain boundary in a silicon polycrystal. *Phys Rev Lett* **115**, 235502.

Tersoff J (1989). Modeling solid-state chemistry: Interatomic potentials for multicomponent systems. *Phys Rev B* **39**(8), 5566–5568.

Thomas JA, Turney JE, Iutzi RM, Amon CH & McGaughey AJH (2010). Predicting phonon dispersion relations and lifetimes from the spectral energy density. *Phys Rev B* **81**, 081411(R).

Togo A & Tanaka I (2015). First principles calculations in materials science. *Scr Mater* **108**, 1–5.

Venkatraman K, Levin BDA, March K, Rez P & Crozier PA (2019). Vibrational spectroscopy at atomic resolution with electron impact scattering. *Nat Phys* **15**, 1237–1241.

Wang CZ, Chan CT & Ho KM (1989). Empirical tight-binding force model for molecular-dynamics simulation of Si. *Phys Rev B* **39**(12), 8586–8592.

Wang CZ, Chan CT & Ho KM (1990). Tight-binding molecular-dynamics study of phonon anharmonic effects in silicon and diamond. *Phys Rev B* **42**(17), 11276–11283.

Yan XX, Liu CY, Gadre CA, Gu L, Aoki T, Lovejoy TC, Delby N, Krivanek OL, Schlom DG, Wu R & Pan XQ (2021). Single-defect phonons imaged by electron microscopy. *Nature* **589**, 65–69.

Zeiger PM & Rusz J (2020). Efficient and Versatile model for vibrational STEM-EELS. *Phys Rev Lett* **124**(2), 025501.

Zeiger PM & Rusz J (2021*a*). Frequency-resolved frozen phonon multislice method and its application to vibrational electron energy loss spectroscopy using parallel illumination. *Phys Rev B* **104**, 104301.

Zeiger PM & Rusz J (2021*b*). Simulations of spatially and angle-resolved vibrational electron energy loss spectroscopy for a system with a planar defect. *Phys Rev B* **104**, 094103.

Ziebarth B, Mrovec M, Elsasser C & Gumbsch P (2015). Interstitial iron impurities at grain boundaries in silicon: A first-principles study. *Phys Rev B* **91**, 035309.

https://doi.org/10.1017/S143192762200040X Published online by Cambridge University Press